Unsteady flow evolution in swirl injector with radial entry. I. Stationary conditions

Shanwu Wang,[a)] Shih-Yang Hsieh, and Vigor Yang
Department of Mechanical and Nuclear Engineering, The Pennsylvania State University, University Park, Pennsylvania 16802

(Received 4 February 2004; accepted 27 January 2005; published online 31 March 2005)

The vortical flow dynamics in a gas-turbine swirl injector were investigated by means of large eddy simulations. The flow enters the injector through three sets of radial-entry, counter-rotating swirl vanes. The formulation treats the Favre-filtered conservation equations in three dimensions along with a subgrid-scale model, and is solved numerically using a density-based, finite-volume approach with explicit time marching. Several methods, including proper orthogonal decomposition, spectral analysis, and flow visualization, are implemented to explore the flow dynamics in the complex three-dimensional flowfields. Various underlying mechanisms dictating the flow evolution, such as vortex breakdown, the Kelvin–Helmholtz instability, and helical instability, as well as their interactions, are studied for different swirl numbers. The flowfield exhibits well-organized motion in a low swirl-number case, in which the vortex shedding arising from shear instabilities downstream of the guide vanes drives acoustic oscillations of the mixed first tangential and first radial mode. The flowfield, however, becomes much more complicated at high swirl numbers, with each sub-regime dominated by different structures and frequency contents. © *2005 American Institute of Physics*. [DOI: 10.1063/1.1874892]

I. INTRODUCTION

Swirl injectors are commonly used in modern gas-turbine engines to achieve efficient and clean combustion. In addition to its primary functions of preparing a combustible mixture and stabilizing the flame, the injector acts as a sensitive element that may generate and modulate flow oscillations in the chamber through the following three mechanisms. First, the internal flow evolution in an injector is intrinsically unsteady and involves a wide variety of structures with different time and length scales. These structures, when convected downstream, can easily interact with the flowfield near the injector exit and modify the local flame-zone physiochemistry. Second, the injector flow dynamics dictate the liquid-sheet breakup and droplet formation processes, and subsequently affect the fuel distribution. Third, the injector flow may interact resonantly with the acoustic waves in the combustor. The coupling often leads to large flow oscillations in the chamber, a phenomenon commonly referred to as combustion instability.[1,2]

Most previous studies on combustion instabilities in liquid-fueled propulsion systems focused either on thermal-acoustic interactions in the chamber using analytical approaches,[3] or on detailed flow evolution and flame dynamics using comprehensive modeling techniques, such as large-eddy simulations.[4–6] The dynamic behavior of an injector was loosely modeled with an acoustic admittance function at the injector exit, whose specific value was treated as an empirical coefficient. Very limited effort was applied to examine the injector internal flow evolution and its response to externally imposed forcing, although liquid-propellant rocket injectors have been investigated using an analytical approach augmented by experimental data.[7]

The purpose of the present work is to remedy this deficiency by developing a comprehensive analysis of turbulent swirling flows in a contemporary gas-turbine airblast injector. Several fundamental mechanisms dictating the flow evolution, including vortex breakdown, the Kelvin–Helmholtz instability, helical instability, and centrifugal instability, as well as their mutual coupling, are carefully investigated. An improved understanding of these fundamental flow phenomena stands out as a prerequisite for successful development of high-performance gas-turbine combustors. The previous studies of injector dynamics using simplified models are far from enough to reveal the flow physics in complex geometries.

The injector considered herein consists of a mixing duct and a fuel nozzle located coaxially at the head end,[8] as shown schematically in Fig. 1. The former includes a center cylindrical passage and two annular passages, which are spaced radially outward from the axial axis. Three radial-entry swirlers, denoted as S_1, S_2, and S_3, and counter-rotating with each other, are located at the entrance. The analysis is based on a large-eddy-simulation (LES) technique, which allows the flowfield to be resolved at a scale sufficient to characterize the detailed flow evolution. Various underlying mechanisms are examined in detail for two different swirl numbers. The study also provides the basis for an exploration of the response of the injector flowfield to external forcing.[9]

[a)]Telephone: +1(814)863-6265. Fax: +1(814)865-3389. Electronic mail: shanwu@psu.edu

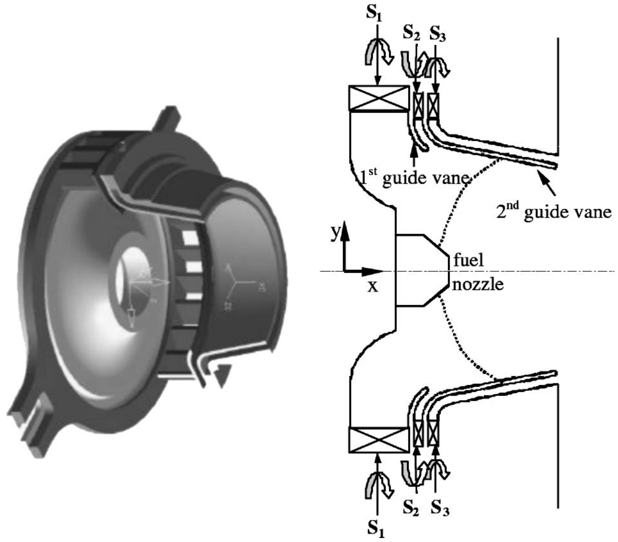

FIG. 1. Schematic of gas-turbine swirl injector with radial entry. Case 1: $S_1=30°$, $S_2=-45°$, and $S_3=50°$; case 2: $S_1=45°$, $S_2=-60°$, and $S_3=70°$.

II. THEORETICAL FORMULATION

A. Favre-filtered governing equations

A large-eddy-simulation technique is developed and implemented in the present work, in which large-scale motions are calculated explicitly, whereas eddies with scales smaller than the grid or filter size are modeled to represent the effects of unresolved motions on resolved scales. The formulation treats the Favre-filtered conservation equations of mass, momentum, and energy in three dimensions, written in the following conservative form:

$$\frac{\partial\bar{\rho}}{\partial t}+\frac{\partial\bar{\rho}\tilde{u}_i}{\partial x_i}=0, \tag{1}$$

$$\frac{\partial\bar{\rho}\tilde{u}_i}{\partial t}+\frac{\partial(\bar{\rho}\tilde{u}_i\tilde{u}_j)}{\partial x_j}=-\frac{\partial\bar{p}}{\partial x_i}+\frac{\partial(\tilde{\tau}_{ij}-\tau_{ij}^{\mathrm{sgs}}+D_{ij}^{\mathrm{sgs}})}{\partial x_j}, \tag{2}$$

$$\frac{\partial\bar{\rho}\tilde{E}}{\partial t}+\frac{\partial[(\bar{\rho}\tilde{E}+\bar{p})\tilde{u}_i]}{\partial x_i}=\frac{\partial(-\tilde{q}_i+\tilde{u}_j\tilde{\tau}_{ij}-Q_i^{\mathrm{sgs}}+\sigma_i^{\mathrm{sgs}}-H_i^{\mathrm{sgs}})}{\partial x_i}, \tag{3}$$

where overbar $(-)$ denotes the spatial-filtering operation and tilde $(\sim)$ the Favre-filtering operation, i.e., $\tilde{f}\equiv\overline{\rho f}/\bar{\rho}$. The variables ρ,u_i,p,E,q_i, and τ_{ij} represent the density, velocity, pressure, specific total energy, heat flux, and viscous stress, respectively. The equation of state for an ideal gas is used. The subgrid-scale (sgs) terms are

$$\tau_{ij}^{\mathrm{sgs}}=\bar{\rho}(\widetilde{u_iu_j}-\tilde{u}_i\tilde{u}_j), \tag{4}$$

$$D_{ij}^{\mathrm{sgs}}=(\overline{\tau_{ij}}-\tilde{\tau}_{ij}), \tag{5}$$

$$Q_i^{\mathrm{sgs}}=(\overline{q_i}-\tilde{q}_i), \tag{6}$$

$$H_i^{\mathrm{sgs}}=\bar{\rho}(\widetilde{Eu_i}-\tilde{E}\tilde{u}_i)+(\overline{pu_i}-\bar{p}\tilde{u}_i), \tag{7}$$

$$\sigma_i^{\mathrm{sgs}}=(\overline{u_j\tau_{ij}}-\tilde{u}_j\tilde{\tau}_{ij}). \tag{8}$$

They are treated by means of the Smagorinsky model for compressible flows proposed by Erlebacher *et al.*[10] because of its reasonable accuracy and simplicity in simulations of turbulent flows in complex geometries. The anisotropic part of the sgs stresses, Eq. (4), is treated using the Smagorinsky model,[11] while the isotropic part, τ_{kk}^{sgs}, is modeled with a formulation proposed by Yoshizawa,[12]

$$\tau_{ij}^{\mathrm{sgs}}-\frac{\delta_{ij}}{3}\tau_{kk}^{\mathrm{sgs}}=-2\nu_t\bar{\rho}\left(\tilde{S}_{ij}-\frac{\delta_{ij}}{3}\tilde{S}_{kk}\right), \tag{9}$$

$$\tau_{kk}^{\mathrm{sgs}}=2\bar{\rho}k^{\mathrm{sgs}}=2C_I\bar{\rho}(D\Delta)^2|\tilde{S}|^2, \tag{10}$$

where

$$\nu_t=C_R(D\Delta)^2|\tilde{S}|,$$

$$\tilde{S}_{ij}=\frac{1}{2}\left(\frac{\partial\tilde{u}_j}{\partial x_i}+\frac{\partial\tilde{u}_i}{\partial x_j}\right),$$

$$k^{\mathrm{sgs}}=\tfrac{1}{2}(\widetilde{u_iu_i}-\tilde{u}_i\tilde{u}_i).$$

The dimensionless quantities C_R and C_I are the compressible Smagorinsky model constants. Yoshizawa[12] proposed an eddy-viscosity model for weakly compressible turbulent flows, using a multi-scale, direct-interaction approximation method, and suggested $C_R=0.012$ and $C_R=0.0066$ based on theoretical arguments. The Van Driest damping function D is used to take into account the inhomogeneities near the wall boundary,[13] and is expressed as

$$D(y^+)=1-\exp[-(y^+/25)^3], \tag{11}$$

where $y^+=u_\tau y/\nu$, $u_\tau=\sqrt{\overline{\tau_w}/\bar{\rho}}$, and $\overline{\tau_w}$ denotes wall stress.

The subgrid energy flux term, H_j^{sgs}, is modeled as

$$H_j^{\mathrm{sgs}}=-\bar{\rho}\frac{\nu_t}{\mathrm{Pr}_t}\frac{\partial\tilde{H}}{\partial x_j}=-\bar{\rho}\frac{\nu_t}{\mathrm{Pr}_t}\left(\frac{\partial\tilde{h}}{\partial x_j}+\tilde{u}_i\frac{\partial\tilde{u}_i}{\partial x_j}+\frac{\partial k^{\mathrm{sgs}}}{\partial x_j}\right), \tag{12}$$

where $\tilde{H}$ represents the filtered specific total enthalpy. The turbulent Prandtl number, Pr_t, takes a conventional value of 0.7.[14] The sgs viscous diffusion term, σ_i^{sgs}, is neglected in the present study due to its small contribution in the energy equation.[15] The nonlinearity of the viscous stress term, D_i^{sgs}, and the heat flux term, Q_i^{sgs}, is invariably neglected.[16]

B. Boundary conditions

The computational domain shown in Fig. 2 includes both the injector interior and an external downstream region in order to provide a complete description of the flow development. The length and diameter of the external region are 15 and 8 times the injector diameter at the exit, respectively. This region is sufficiently large to minimize the effects of boundary conditions on the calculated injector flow evolution. The flow is subsonic throughout the entire domain.

The boundary conditions are specified according to the method of characteristics. At the inlet, the pressure is determined using a one-dimensional approximation to the momentum equation in the direction normal to the inlet bound-

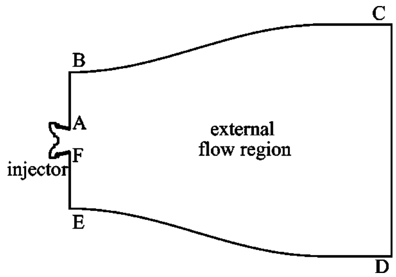

FIG. 2. Overall computational domain.

ary. The mass flux, total temperature, axial velocity, and flow angle are specified. Turbulence is provided by superimposing broadband noise with a Gaussian distribution on the mean velocity profile with an intensity of 8% of the mean quantity. The effect of the inlet turbulence on the flow development seems to be modest due to the strong shear layers and high-intensity turbulence generated in the flowfield, which overshadow the influence of the incoming turbulence.

At the downstream boundary (line *CD* in Fig. 2), extrapolation of primitive variables from the interior may cause undesired reflection of waves propagating into the computational domain. Thus, the non-reflecting boundary conditions based on the characteristic equations, as proposed by Poinsot and Lele,[17] are applied. A reference pressure, p_∞, is utilized to preserve the average pressure in the computational domain using small amplitude acoustic waves. In the present study, a uniform distribution of p_∞ is employed, since the azimuthal velocity at the exit is relatively small.

The no-slip, adiabatic condition is applied along all the solid walls inside of the injector. The slip, adiabatic condition is used along the boundaries *AB* and *EF* of the external computation domain. Because the flow is exhausted to an ambient condition after passing through the injector, the surrounding air may be entrained into the computational domain. At the radial boundaries (lines *BC* and *DE*), the pressure, total temperature, and axial velocity are specified. The laws of conservation of mass and angular momentum are employed to determine the radial and azimuthal velocities, respectively.

III. NUMERICAL METHOD

The theoretical formulation outlined above is solved numerically by means of a density-based, finite-volume methodology. Wang[18] recently extended the approaches of Fabignon *et al.*[19] and Apte and Yang[20] to study the numerical accuracy of several explicit time-marching algorithms within the context of LES. The numerical dissipation arising from the discretization of convective terms and artificial viscosity were assessed by introducing a reference turbulent kinetic energy spectrum obtained from isotropic turbulence theory. Results indicated that the numerical dissipation of a density-based approach in simulations of turbulent flows at low Mach numbers is insensitive to the specific time-marching scheme selected. This may be attributed to the fact that the maximum allowable time step for a density-based scheme is much smaller than the turnover time of grid-sized eddy, due to the large disparity in the eigenvalues for low Mach-number flows. For example, the spectrum of turbulent kinetic energy calculated using the Adam–Bashforth predictor-corrector scheme is almost identical to that calculated using a four-step Runge–Kutta scheme, as will be shown later. In light of this finding, the present work employs the Adam–Bashforth scheme for temporal discretization, to save computing time. Spatial discretization of the convective terms is achieved using a fourth-order central difference scheme along with sixth-order artificial dissipation in generalized coordinates.[21]

To minimize the contamination originating from numerical dissipation, the coefficient of the sixth-order dissipation terms was carefully selected to be $\epsilon_6=0.001$. When the SGS terms were turned off, unphysical oscillations took place in the flowfield. For example, at the location of $x=21$ mm, $y=14$ mm, and $z=0$ mm in the case with a high swirl number to be discussed later, the axial velocity in the main flow passage fluctuated between −5 and 100 m/s, whereas the long-time mean velocity was 70 m/s. A further decrease in the numerical dissipation coefficient resulted in an overflow of the calculation. When the SGS terms were activated, the solution was stable even if the numerical dissipation was reduced by half. This suggests that the numerical method and grid resolution employed in the present study did not give rise to a dissipative solution.

A multi-block domain-decomposition method is implemented to facilitate parallel processing in a distributed computing environment using the Message Passing Interface (MPI) library. The overall approach has been validated by Apte and Yang,[20,22] Huang *et al.*,[23] and Lu *et al.*,[24] against a variety of vortical flow problems to establish its credibility.

The code was further validated against two flow configurations with complex geometries. The first study dealt with a LES of turbulent swirling flows injected into a dump chamber,[24] simulating the experiments by Favaloro *et al.*[25] A swirler with 12 circular inlet guide vanes is located at 50.8 mm upstream of the dump plane. The temperature and pressure at the entrance are 300 K and 1 atm, respectively. The height of the backward-facing step is $H=25.4$ mm. The Reynolds number is 1.25×10^5 based on the inlet diameter of 101.6 mm and centerline velocity 19.2 m/s. Owing to the lack of reliable data for the flow conditions at the entrance, the inlet velocity profiles were tuned to match the experimental data at the first measurement position ($x/H=0.38$). Reasonable agreement between simulations and measurements was obtained in terms of mean velocity components and turbulence intensities. The second validation case treated the flow evolution in a twin-swirler injector (i.e., General Electric CFM56 aero-engine injector). The system includes eight counterclockwise elliptical primary swirl jets, ten clockwise secondary swirl vanes, a venturi, and a flare. The inlet flow pressure and temperature are 1 atmosphere and 291 K, respectively. The diameter, $D_0=27$ mm, and mean axial velocity, $U_0=30$ m/s, at the downstream side of the secondary swirl vanes are selected as the characteristic length and velocity, respectively. The corresponding Reynolds number is 5.4×10^4. Excellent agreement was obtained with experimental data. The length of the central recircula-

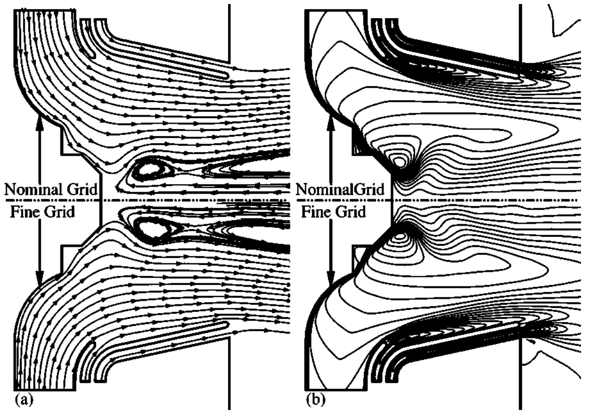

FIG. 3. Comparison of flowfields simulated using different grids. (a) Pseudo-streamlines based on mean axial and radial velocities; and (b) contours of mean azimuthal velocity. Contour levels between −90 and 160 m/s with increment of 10 m/s. High swirl number (S=0.49).

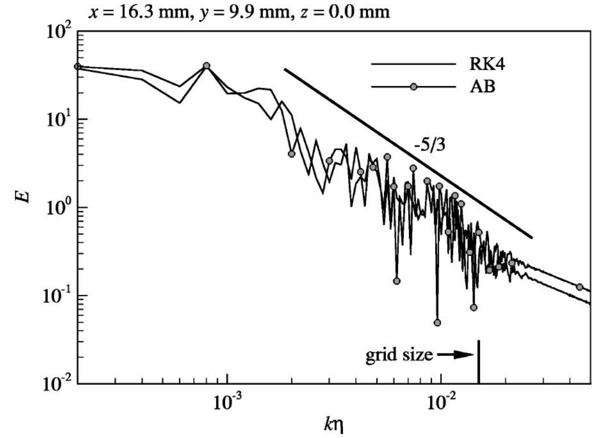

FIG. 4. Spectra of turbulent kinetic energy at x=16.3 mm, y=9.9 mm, and z=0.0 mm.

tion zone is identical to the measured value. The maximum discrepancies of mean velocity components and turbulence intensities between simulations and measurements are, respectively, about 0.1 and 0.05 U_0 at the injector exit and less than 0.05 and 0.02 U_0 at an axial location one injector diameter downstream of the exit.

IV. FLOW CONFIGURATION AND GRID SYSTEM

The mixing duct in the injector, shown in Fig. 1, has a diameter of D_0=32 mm at the exit. Two different sets of swirl vanes are considered. The low swirl-number case has swirl vane angles of S_1=30°, S_2=−45°, and S_3=50°, and the high swirl-number case has S_1=45°, S_2=−60°, and S_3=70°. The corresponding swirl numbers, defined as the ratio of the axial flux of angular momentum to the production of the axial flux of axial momentum and the injector diameter, are 0.35 and 0.49, respectively, at the injector exit. The baseline flow condition includes an ambient pressure of 1 atm, an inlet temperature of 293 K, and a mass flow rate of 0.077 kg/s. The Reynolds number based on the diameter and the bulk axial velocity at the exit is 2×10^5.

A three-dimensional grid system is generated by rotating a two-dimensional grid around the centerline. The entire grid system has two million cells, of which 0.9 million grids are located within the injector. The mean grid size within the injector interior is around 0.2 mm, which is sufficient to resolve the turbulence length scales in the inertial sub-range of the turbulent energy spectrum, as will be discussed later. The spatial resolution near the wall falls in the range of $3 < y^+ < 10$, which is roughly within the viscous sub-layer region.

A grid independence study was performed as part of the validation procedure. A refined mesh with 3.2 million grid points was considered. The node numbers in the axial and radial directions were increased by 20% and 30%, respectively. The average grid size inside the injector was reduced by 17%. The external computational domain was also expanded to examine the effects of the outflow boundary conditions. Figure 3 shows the calculated streamlines and azimuthal velocity field on a longitudinal plane for the two grid systems. With an increase of 50% computational cells, the mean velocity components and turbulence intensities only vary by 1% and 2% of the bulk velocity at the injector exit, respectively. The frequency spectrum of the pressure field indicates an identical dynamic behavior. The grid system adopted in the present work appears to be credible.

A total of 54 computational blocks are used to facilitate parallel processing. The physical time step is 5×10^{-5} ms and the maximum CFL number is 0.8. For each case, the calculation is first conducted for an extended period until the flowfield reaches its stationary state. The time stamp is then reset, and data are collected for more than 30 flow-through times (i.e., 20 ms) to obtain statistically meaningful turbulence properties.

Figure 4 shows the spectra of the turbulent kinetic energy at a probe in the main flow passage, calculated using both the Adam–Bashforth predictor-corrector (AB) and the four-step Runge–Kutta (RK4) schemes. The wave number is denoted by k. The Kolmogorov scale ($\eta \sim D_0 \,\mathrm{Re}^{-3/4}$) is 3 μm and the Taylor scale ($l_T \sim D_0 \,\mathrm{Re}^{-1/2}$) 70 μm, based on the Reynolds number. Here Taylor's hypothesis[26] is applied to approximate spatial correlations with temporal correlations, since the original data are the velocity-time traces at single points, from which spatial correlations cannot be directly derived. An accuracy conversion based on this hypothesis is limited to homogeneous turbulence with small intensity.[27] Although the present study does not satisfy this strict constraint, it still can be regarded as a good reference for data analysis. The large scales on the order of the characteristic length, D_0, are around $\eta/D_0 \sim 10^{-4}$, and most of turbulent kinetic energy is carried by flow motion with normalized scales less than 10^{-3}, as evidenced in Fig. 4. The result follows the Kolmogorov–Obukhov spectrum (−5/3 law) in the high wave number regime, and the grid size employed in the present study is located in the inertial sub-range of turbulence.

V. RESULTS AND DISCUSSION

Figure 5 shows snapshots of the vorticity-magnitude fields on two cross sections for both the low and high swirl

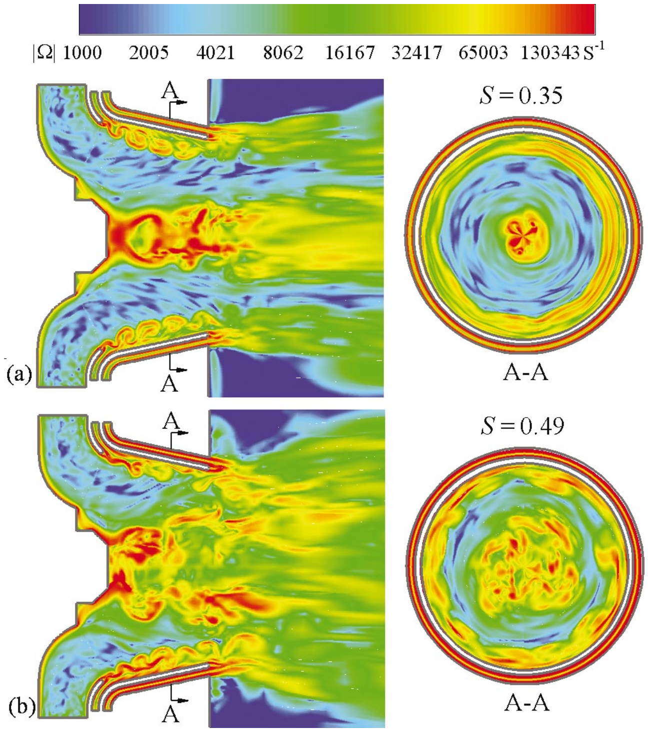

FIG. 5. (Color). Snapshots of vorticity magnitude contours. (a) Low swirl number and (b) high swirl number.

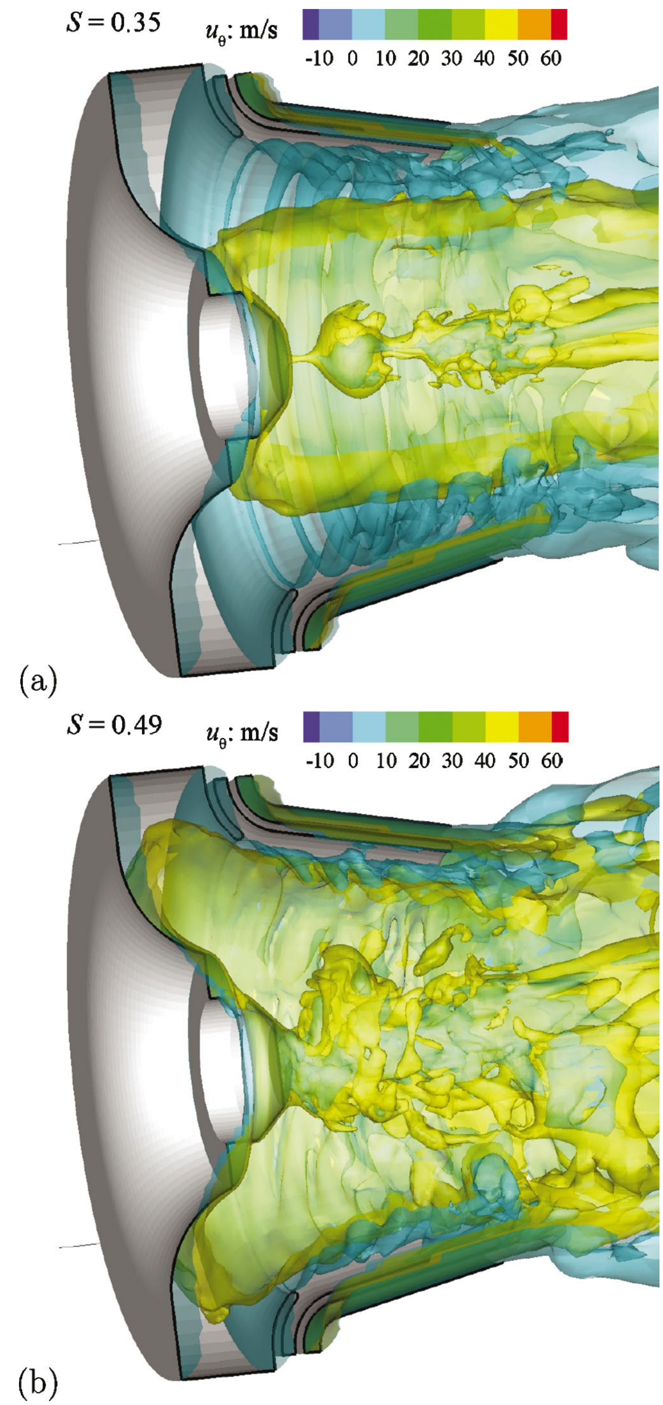

FIG. 6. (Color). Instantaneous iso-surfaces of azimuthal velocities at $u_\theta = 10$ and 50 m/s. (a) Low swirl number and (b) high swirl number.

numbers. The flow evolution exhibits several distinct features, as follows. First, the flowfield is essentially irrotational after passing through the radial-entry swirl vanes. The weak vorticity downstream of the inlet arises from the imposed broadband noise simulating the inflow turbulence. Strong vorticity then develops in the boundary layers near the walls, and in the regions downstream of the guide vanes and the centerbody, due to the large velocity difference in the shear layers.

Second, when the flow travels downstream of the centerbody, the strong swirling motion and its associated centrifugal force produces large radial pressure gradients, which then induce a low-pressure core around the centerline. As the flow expands and the azimuthal velocity decays with the axial distance, the pressure is recovered. A positive pressure gradient is consequently generated in the axial direction and leads to the formation of a central recirculating flow, a phenomenon commonly referred to as vortex breakdown or vortex burst. The resultant flow detachment from the rim of the centerbody gives rise to a vorticity layer, which subsequently rolls, tilts, stretches, and breaks up into small eddies. These small vorticity bulbs interact and merge with the surrounding flow structures while being convected downstream. The entire process is highly unsteady and involves a wide range of length and time scales.

Third, because of the opposition of the swirler vane angles, two counter-rotating flows with different velocities in the streamwise and azimuthal directions merge at the trailing edges of the guide vanes. Vortices are generated in the shear-layer regions and shed downstream sequentially due to the Kelvin–Helmholtz instabilities. In comparison with the vortex-breakdown-induced central recirculating flow, the flow structures associated with the periodic vortex shedding in the outer region are small and well organized. The shear-layer instability, along with the helical and centrifugal instabilities, induces large asymmetric structures on the transverse plane.

Finally, the aforementioned flow structures in various parts of the injector and their underlying mechanisms interact and compete with each other. When the swirl number changes, the dominant instability mode may switch correspondingly. A detailed analysis of these phenomena will be delivered in the following sections.

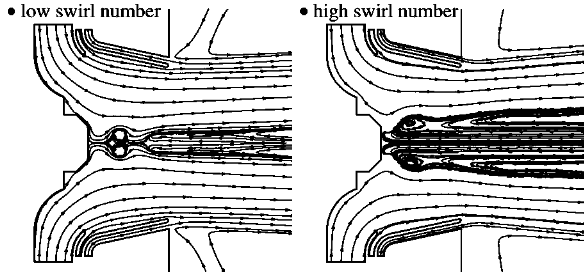

FIG. 7. Streamlines of mean flowfields for swirl numbers of $S=0.35$ and 0.49.

A. Vortex breakdown

Much insight into the vortex breakdown in the core flow region can be obtained from the iso-surfaces of the azimuthal velocity shown in Fig. 6. In the low swirl-number case, a stable bubble type of vortex breakdown is clearly observed in the downstream region of the centerbody, whereas a much more complex structure prevails at the high swirl number. The streamlines and the axial velocities of the mean flowfields given in Figs. 7 and 8, respectively, reveal the formation of a central toroidal recirculation zone in this region quantitatively. As the swirl number increases, the size of the recirculation zone becomes greater accordingly. The stagnation point of the vortex breakdown moves upstream for an equilibrium position and finally reaches the centerbody. The local flow development depends on the relative magnitudes of the downward momentum inertia of the incoming flow and the outward flow motion arising from the centrifugal force. Although the former remains almost the same due to the fixed inlet mass flow rate employed in the present study, the weaker centrifugal force in the low swirl-number case causes the incoming flow to penetrate all the way to the core region, as evidenced in Fig. 7. The ensuing flow structure bears a close resemblance to a tornado near the ground where a large accumulation of vorticity in the center region takes place, a kind of *collapse* of the swirling flow.[28]

The difference in the flow topology affects the pressure and velocity development considerably. The situation can be explained based on the momentum balance in the radial direction as follows:

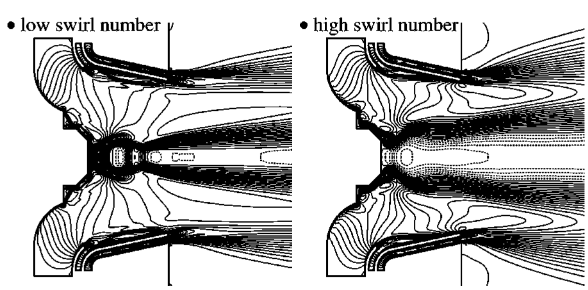

FIG. 8. Contours of mean axial velocity for swirl numbers of $S=0.35$ and 0.49. Contour levels between −30 and 125 m/s with increment of 5 m/s. Solid lines: positive values; dashed lines: negative values.

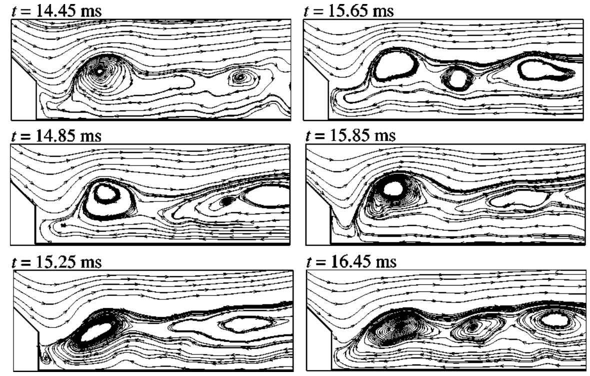

FIG. 9. Close-up views of streamlines downstream of centerbody for high swirl-number case of $S=0.49$. Flowfields spatially averaged in azimuthal direction. The time interval between pictures is not constant.

$$\frac{\partial p}{\partial r} \sim f_c \sim \frac{\rho u_\theta^2}{r}, \tag{13}$$

where f_c denotes the centrifugal force and u_θ the azimuthal velocity. The maximum mean azimuthal velocities and their corresponding radial locations are 157 m/s at 5.0 mm for the high swirl number and 151 m/s at 2.3 mm for the low swirl number, respectively, near the centerbody. The smaller radius (i.e., 2.3 mm) in the low swirl-number case results in a minimum pressure of 78 kPa, which is even lower than that in the high swirl-number case, 88 kPa. This phenomenon contradicts the usual assumption that a stronger swirling flow induces a lower pressure in the core region. Not only swirl strength but also flow topology determine the local flow evolution. At the same time, the no-slip condition results in relatively high pressure in the wall region. The resultant negative pressure gradient in the axial direction leads to a strong jet along the centerline downstream of the centerbody. The flow accelerates rapidly from 0 to 125 m/s within 2.2 mm.[18] This phenomenon was not observed in the high swirl-number case. Instead, a large central recirculating flow is established in the same region.

The formation of the central toroidal recirculation zone, which is attached to the centerbody in the high swirl-number case, mainly results from the vortex breakdown. The wake downstream of the centerbody exerts a very limited influence on the flow reversal since it is not observed even in the low swirl-number case. Two points should be mentioned here. First, in general, both the swirl and the wake contribute to the generation of a flow reversal. A slight change in the centerbody geometry may greatly alter the local flow development and the injector dynamics. Care must therefore be exercised in designing the injector configuration. Second, the streamline topology shown in Fig. 7 dictates the effective flow-passage area, which plays an important role in determining the injector dynamics, as will be elaborated later.

The temporal evolution of the flowfield permits insight into the vortex breakdown phenomenon. Figure 9 shows instantaneous streamlines on a longitudinal plane, spatially averaged in the azimuthal direction, at various times during a typical flow evolution period for the high swirl-number case. Uneven time intervals between frames were chosen to show

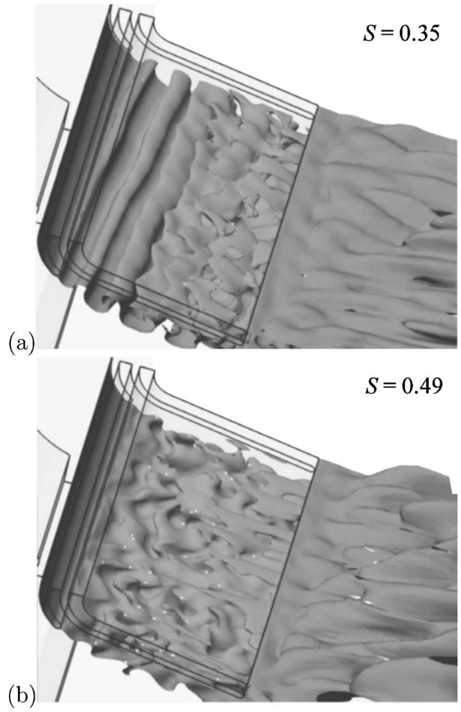

FIG. 10. Iso-surface of azimuthal velocity at $u_\theta = 10$ m/s in azimuthal phase space ($\theta = 0° - 360°$). (a) Low swirl number and (b) high swirl number.

the important phases of the oscillation. Obviously, the spatially averaged flow structures are more distinguishable than those of the original three-dimensional flowfield, which is too complex to allow an effective analysis. Two large vortices exist in the region downstream of the centerbody, and evolve in two different forms. First, between 14.45 and 14.85 ms, a small vortex separates from its parent structure, travels downstream, and eventually coalesces with the large vortex located in the downstream region. In a later stage, between 15.25 and 15.85 ms, a small vortex is generated in front of the array of vortices and the large vortex, which is normally anchored at the centerbody, is detached, causing a switch in the flow topology. The instantaneous flow pattern at 15.85 mm is considerably different from its time-mean counterpart, and bears a close resemblance to the situation for the low swirl-number case, in which a strong wall jet exists in the wake of the centerbody and the incoming flow can penetrate deeply into the core region. The temporal variation in the vortical structure affects the injector characteristics through its influence on the effective flow-passage area.

B. Outer shear-layer instability

Vortex shedding arising from the Kelvin–Helmholtz instabilities in both the axial and azimuthal directions takes place at the trailing edges of the guide vanes. Figure 10 shows the iso-surfaces of the azimuthal velocity at 10 m/s in the phase space, i.e., the physical domain is unwrapped in the azimuthal direction, illustrating the shear-layer evolution in the outer region of the injector flowfield. For the low swirl-number case, small-amplitude instability waves are initiated as soon as the flows merge at the rim of the guide vane. These waves then develop to large-scale billows, become distorted into hairpin structures, and finally break up into small eddies in the downstream region of the mixing layer due to turbulent mixing.

The dominant frequency of the vortex shedding due to the Kelvin–Helmholtz instability in the streamwise direction can be estimated using the formula given in Ref. 29,

$$f_n = \mathrm{St}\frac{\overline{U}}{\theta}, \tag{14}$$

where the Strouhal number, St, is 0.044–0.048 for turbulent flows. In the present study, the mean velocity, $\overline{U}$, is 50 m/s, and the momentum thickness of the shear layer, θ, is around 0.2 mm for both swirl numbers. The frequency of the most unstable mode, f_n, is estimated to be 1×10^4 Hz. This value is comparable with the numerically calculated instability frequency of 13 000 Hz using the spectral analysis described in Sec. V E, further demonstrating that the outer shear flow dynamics is dictated by the Kelvin–Helmholtz instability in the streamwise direction in the low swirl-number case.

The situation is vastly different in the high swirl-number case. As a result of the strong shear force and the associated Kelvin–Helmholtz, helical, and centrifugal instabilities in the azimuthal direction, the flow becomes highly disordered

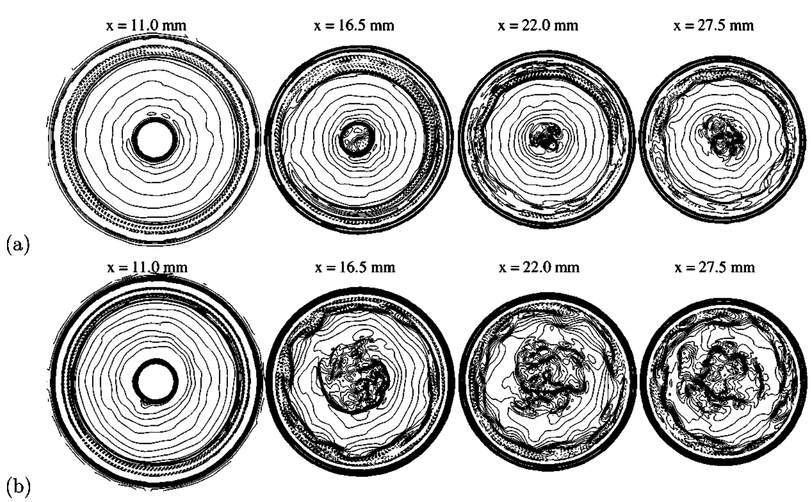

FIG. 11. Snapshots of azimuthal velocity fields on four transverse cross sections, contour levels between −70 and 120 m/s with increment of 10 m/s. Solid lines: positive values; dashed lines: negative values. (a) Low swirl number and (b) high swirl number.

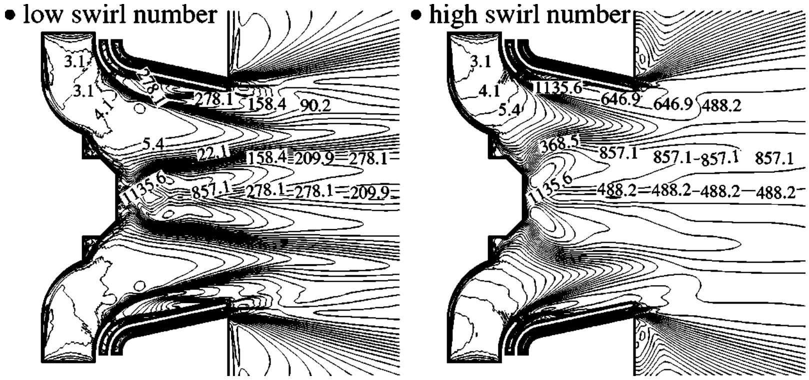

FIG. 12. Distributions of turbulent kinetic energy at swirl numbers of $S=0.35$ and 0.49. Contour levels between 1 and $3500\ \mathrm{m^2/s^2}$ with an exponential distribution.

soon after the incoming streams merge together in the region downstream of the guide vanes. The interaction between the outer shear layer and the central toroidal recirculating flow also contributes to the eddy breakup and mixing processes.

The flow evolution in the azimuthal direction, as shown in Fig. 11, clearly indicates the existence of an outer shear layer due to the counter-rotating flows through the first and second passages and a center recirculating flow induced by the vortex breakdown. For the low swirl-number case, the azimuthal velocity remains almost uniform up to $x=11$ mm, in spite of the small-scale turbulence embedded in the inlet flow. Large organized structures then develop under the effect of the Kelvin–Helmholtz instability when the incoming streams merge together. The situation becomes more obvious for the high swirl-number case. The center recirculating flow even intersects the outer shear layer, causing a complex flowfield near the injector exit.

C. Helical instability

In spite of the flow symmetry at the inlet, periodic flow oscillations develop in the azimuthal direction due to the strong shear force in this direction. To facilitate discussion, each flow variable can be expressed using a Fourier series in the cylindrical coordinate system (x,r,θ),

$$f(x,r,\theta,t)=\sum_{m=\infty}^{-\infty} f_m(x,r,t)\exp(im\theta), \tag{15}$$

where m is the wave number in the azimuthal direction, and f_m the Fourier coefficient. $m=0$ represents the axisymmetric mode, and the others $(m\neq 0)$ the helical modes. As will be shown later based on proper-orthogonal-decomposition (POD) analysis, the $m=-1$ helical mode dominates the flowfield at $x=15$ mm in the low swirl-number case, suggesting that the helical wave rotates in the opposite direction of the swirling flow. Lessen *et al.*[30] and Martin and Meiburg[31] found that the counter-rotating helical waves $(m<0)$ are more unstable in swirling jets. The helical-mode oscillation propagates in the azimuthal direction at a speed much faster than that of the mean flow.

Helical motions are not so evident in the high swirl-number case. The interaction between the center recirculating flow and the outer shear layer gives rise to a complex flow structure that tends to suppress the prevalence of simple, well-defined harmonic oscillations.

D. Interaction and competition of instability modes

As mentioned above, three major flow mechanisms, i.e., vortex breakdown, Kelvin–Helmholtz instability, and helical instability, exist and interact with each other within the injector. The specific type of coupling depends on the swirl number and can be classified into two categories. First, the outer shear-layer may interact with the large disorganized structures arising from the evolution of the central recirculating flow when the swirl number exceeds a threshold value, as evidenced in Fig. 5. The interaction usually increases with increasing swirl number and varies within each flow evolution period. The vortex shedding tends to be more organized when the center recirculation zone shrinks, and vice versa. The spatial distributions of turbulent kinetic energy, shown in Fig. 12, also demonstrate this interaction. The turbulent kinetic energy in the central recirculation zone and the wake of the guide vanes is much greater than that in the rest of the domain because of vigorous vortical motions in these regions. The two shear layers are distinctly separate in the low swirl-number case, but merge in the high swirl-number case. Since fuel is delivered into the injector from the centerbody, the high turbulence intensity in this region can significantly enhance the atomization of the injected liquid fuel. At the same time, the strong shear stress in the downstream region of the second guide vane promotes rapid mixing between the air and the fuel impinging and accumulating on the second guide vane.

In the second type of flow coupling, the instability waves in the axial and azimuthal directions in the outer shear layer compete with each other. In the low swirl-number case, the streamwise instability dominates the shear-layer evolution; therefore, the billow structures and subsequent hairpin vortices prevail in the flowfield. In the high swirl-number case, the development of the billows is suppressed and flow structures are severely distorted by the azimuthal flow instabilities.

Several other competing mechanisms may also exist in the flowfield, such as the one involving the Kelvin–Helmholtz and centrifugal instabilities. Swirling flows usually result in an unstable radial stratification, thereby leading to centrifugal instability,[31] which is enhanced by a higher azimuthal velocity gradient and further influences the streamwise Kelvin–Helmholtz instability in the outer shear layer, as shown in Fig. 11.

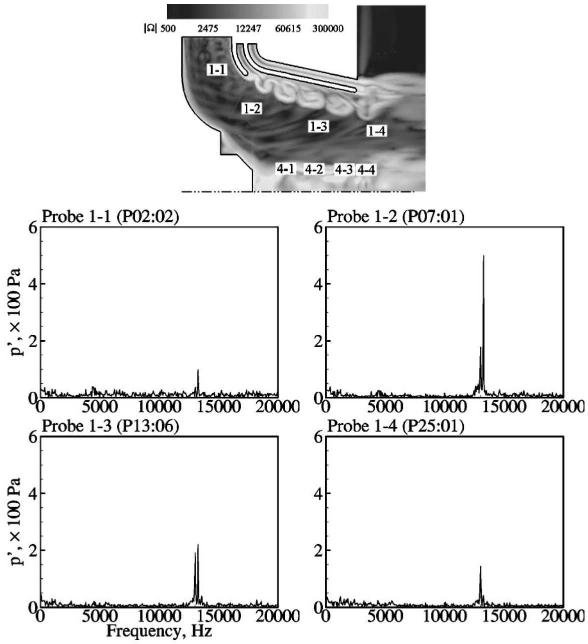

FIG. 13. Frequency spectra of pressure oscillations along main flow passage, low swirl number ($S=0.35$).

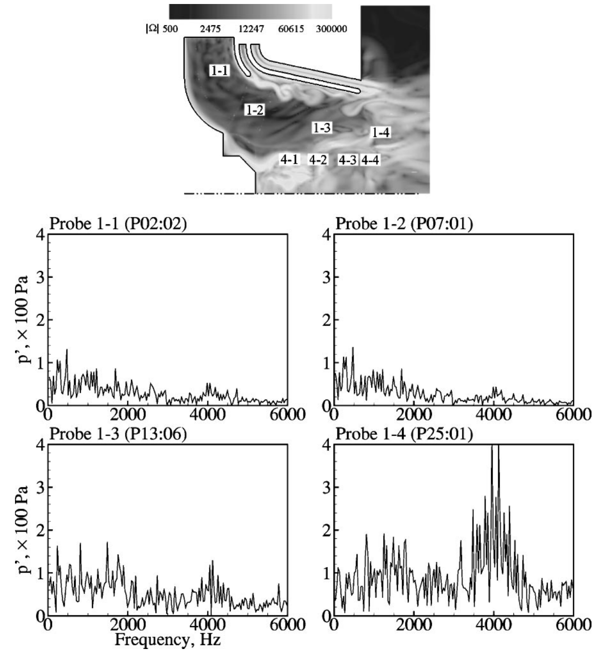

FIG. 15. Frequency spectra of pressure oscillations along main flow passage, high swirl number ($S=0.49$).

E. Spectral analysis

The injector dynamics involve an array of intricate flow processes characterized by a wide range of time and length scales. Quantitative information can be obtained using spectral and proper-orthogonal-decomposition analyses. To this end, extensive effort was made to conduct measurements of flow properties at 626 locations.

Figure 13 shows the frequency spectra of pressure oscillations along the main flow passage for the low swirl-number case. A dominant frequency of 13 000 Hz is clearly observed, corresponding to the most amplified mode of the shear-layer instability downstream of the first guide vane. The oscillation reaches its maximum at probe 1-2 where the shear-layer structure arising from the Kelvin–Helmholtz instability is highly organized. As the flow travels downstream, the development of the hairpin vortices reduces the flow coherence in the azimuthal direction. This effect, along with the growth of vortices in the shear layer, results in a decreased amplitude of flow oscillation at probe 1-4. Figure 14 shows the spectral contents in the outer region of the central recirculation zone. A dominant frequency of 5783 Hz is observed, corresponding to the precession of the vortex core (PVC). The phenomenon is confirmed by visual inspection of the flow evolution data. Although the long-time mean flowfield associated with vortex breakdown is axisymmetric, the instantaneous flowfield is highly time-dependent. PVC is one of the primary unsteady flow motions when the vortex breakdown occurs in the high-Reynolds-number flow regime, as in turbulent swirling flows in cyclone chambers and combustion devices. It is normally located in the boundary of the

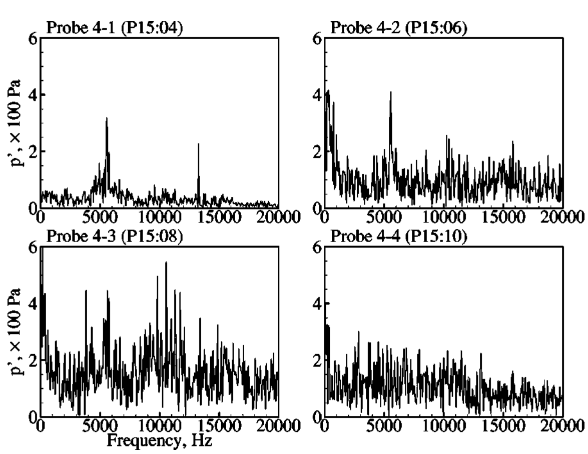

FIG. 14. Frequency spectra of pressure oscillations in outer region of central recirculation zone, low swirl number ($S=0.35$).

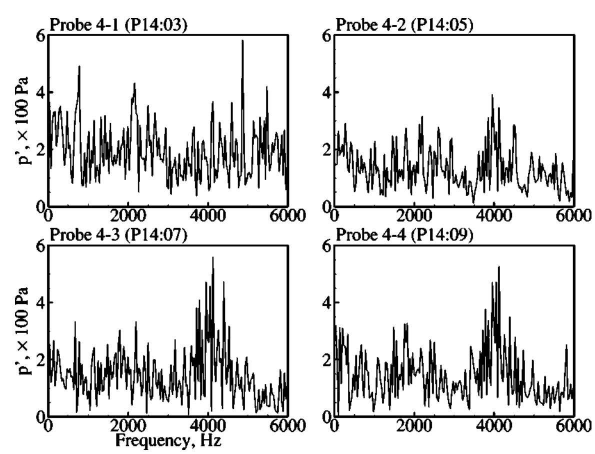

FIG. 16. Frequency spectra of pressure oscillations in outer region of central recirculation zone, high swirl number ($S=0.49$).

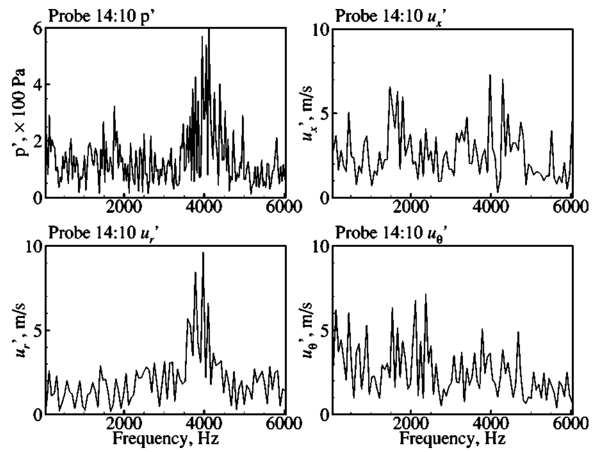

FIG. 17. Frequency spectra of pressure and velocity oscillations within central recirculation zone (x=28.5 mm, y=5.7 mm, z=0.0 mm), high swirl number (S=0.49).

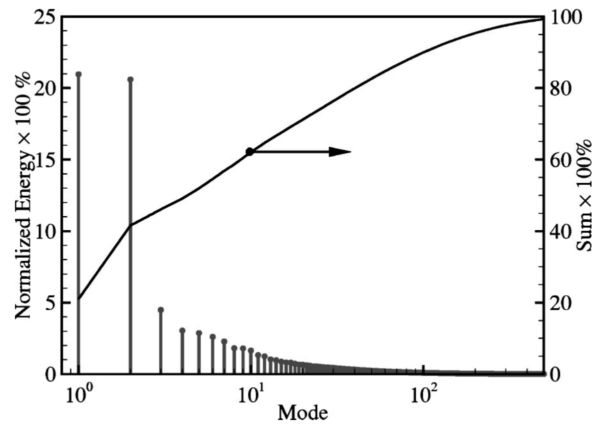

FIG. 18. Energy distribution of POD modes on longitudinal (x–r) plane, low swirl number (S=0.35).

recirculation zone between the zero velocity and the zero streamline.[32,33] In the downstream region, turbulent diffusion and flow expansion prevail.

The flow motion becomes broadband in nature, and no dominant oscillation can be found. The situation is qualitatively different for the high swirl-number case, as shown in Figs. 15 and 16. As a consequence of the strong interactions between the outer shear layer and the central recirculation zone, the spectral content of the flowfield becomes very rich, and is characterized by several different frequencies in various regions. A low-frequency mode around 500 Hz dominates the flow oscillations near the inlet (probes 1-1 and 1-2), whereas high-frequency modes around 4000 Hz prevail in the downstream region (probe 1-4). The former may be attributed to the flow displacement effect of the central recirculation zone, as evidenced in Fig. 9. The occurrence of the 4000 Hz oscillation at the injector exit can be better explained by considering the flow development along the boundary of the central recirculation zone in Fig. 16 (see probes 4-1 through 4-4). A harmonic around 1500 Hz is observed in the mixing layer downstream of the first guide vane and its amplitude increases in the further downstream region. This frequency, as indicated in subsequent work,[9] corresponds to the resonance frequency of the injector in response to external forcing at a high swirl number. The prevalence of distinct frequencies in different regions suggests that the flow instability mechanisms vary in different regions, a phenomenon consistent with Martin and Meiburg's expectation.[31]

Figure 17 shows the frequency spectra of the velocity and pressure oscillations within the central recirculation zone (x=28.5 mm, y=5.7 mm, z=0.0 mm) for the high swirl-number case. The radial velocity fluctuation is intimately coupled with the pressure oscillation compared with the other two velocity components. A major factor contributing to this phenomenon is the large radial pressure gradient caused by the swirling flow. A small velocity disturbance in the radial direction, u_r', results in a relatively large pressure disturbance, p'. Most of the past research focused on the axial and azimuthal velocity fields, instead of the radial velocity, due to their overwhelmingly large values in a swirling flow. The present result, however, indicates that the fluctuations in the radial direction may dominate the unsteady velocity evolution, and play an important role in driving pressure oscillations.

F. Proper orthogonal decomposition analysis

The injector dynamics were further explored using the proper orthogonal decomposition (POD) technique, which extracts energetic coherent structures from the calculated flowfields. For a given flow property, $f(\mathbf{x},t)$, the POD analysis can determine a set of orthogonal functions φ_j, j=1, 2, …, such that the projection of f onto the first n functions

$$\hat{f}(\mathbf{x},t) = \overline{f(\mathbf{x})} + \sum_{j=1}^{n} a_j(t)\varphi_j(\mathbf{x}) \tag{16}$$

has the smallest error, defined as $E(\|f-\hat{f}\|^2)$. Here, $a_j(t)$ represents the temporal variation of the jth mode, and $E(\cdot)$ and $\|\cdot\|$ denote the time average and a norm in the L^2 space, respectively. The function f can be extended to a vector, $\mathbf{F}=[u,v,w,p]^T$, by introducing an appropriate inner product on $\mathbf{F}$. A more complete discussion of this subject can be found in Refs. 34 and 35.

Because of the limitations of data storage for the calculated flowfields over an extended time period, the POD analysis was only conducted for the velocity fields on one longitudinal and two transverse planes. A total of 850 snapshots spanning a time period of 8.5 ms and 1000 snapshots over 10 ms were recorded for the low and high swirl-number cases, respectively. The temporal resolution is 10^{-2} ms and the corresponding cutoff frequency is 5×10^4 Hz. The inner product of functions, $\mathbf{F}$, is defined as the kinetic energy and the method of snapshots is implemented to compute the POD modes.

1. Low swirl number

Figure 18 shows the energy distribution of the POD modes on a longitudinal (x–r) plane for the low swirl-number case. Here the energy of the jth mode, E_j, is defined as

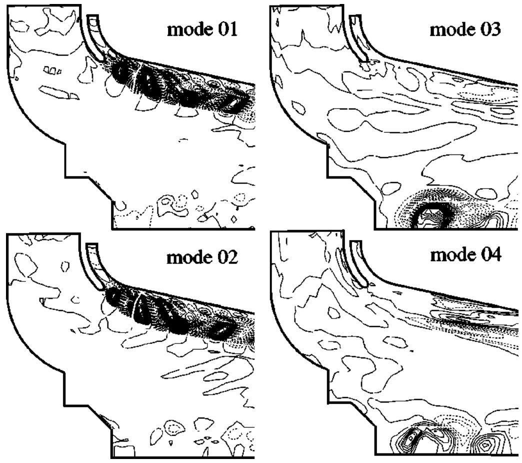

FIG. 19. Spatial distributions of first four POD modes (azimuthal velocity fields) on longitudinal (x–r) plane, low swirl number (S=0.35). Contour levels between −1000 and 1000 m/s with increment of 50 m/s. Solid lines: positive values; dashed lines: negative values.

$$E_j \equiv E(\|a_j(t)\varphi_j(\mathbf{x})\|^2). \tag{17}$$

Figure 19 shows the spatial distributions (i.e., mode shapes, ϕ_j) of the first four POD modes. The first two modes have almost the same energy level (21.0% and 20.6%) and account for more than 40% of the total energy of the fluctuating velocity field. This suggests that the flow structure due to vortex shedding in the outer shear layer is dominant in the streamwise direction. The phase differences between the first two modes in both time and space are $\pi/2$. The local mean streamwise velocity, U_v, wavelength, λ_v, and frequency, f_v, satisfy the relation of $f_v \sim U_v/\lambda_v$ along the outer shear layer, suggesting the existence of a well-organized vortical wave in the wake of the first guide vane. Here the wavelength is defined as the distance between the two adjacent coherent structures. The frequency spectra of the time-varying coefficients, $a_j(t)$, of the first six modes are shown in Fig. 20. The dominant frequency of the first two modes is $f_0 = 1.3 \times 10^4$ Hz. Another important frequency of 5.7×10^3 Hz is observed in the third mode, which corresponds to the precession of the central recirculating flow based on the visual evidence.

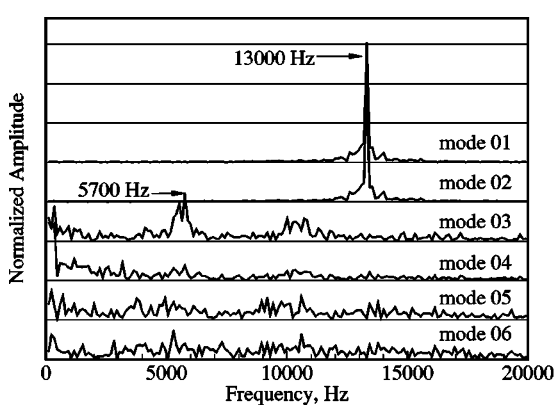

FIG. 20. Frequency spectra of temporal variations of first six POD modes, low swirl number (S=0.35).

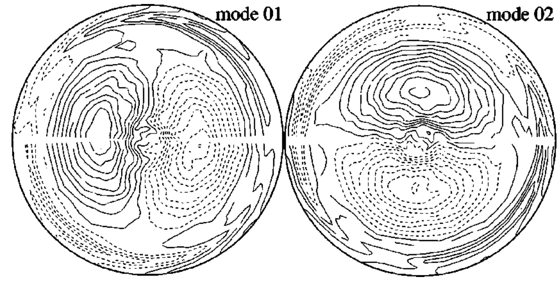

FIG. 21. Spatial distributions of first two POD modes (pressure field) on transverse plane at x=15 mm, low swirl number (S=0.35). Contour levels between −18 000 and 18 000 Pa with increment of 2000 Pa. Solid lines: positive values; dashed lines: negative values.

Figure 21 shows the pressure field of the first two POD modes on the transverse plane at x=15 mm. The dominant frequency is $f_0 = 1.3 \times 10^4$ Hz, according to the spectral analysis of the time-varying coefficients. The mode shape bears a close resemblance to the mixed first-tangential (1T) and first-radial (1R) mode of the acoustic motion. If the injector interior geometry is approximated with a cylinder with an average diameter of 19 mm, then a simple acoustic modal analysis, without taking into account the mean-flow effects, indicates that the eigen-frequency of the 1T/1R acoustic mode is 1.5×10^4 Hz, which is close to f_0, assuming the speed of sound to be 340 m/s for air at the room condition. The result clearly shows that the shear-layer instability can easily resonate with the acoustic field in the injector and consequently lead to large excursions of flow oscillations, provided their characteristic time scales match. Another important factor dictating the vortico-acoustic interaction is the spatial location of the shear layer with respect to the acoustic mode shape. An acoustic wave can be excited more efficiently if the driving source is located at its antinodal position. Similar phenomena were also observed by Huang *et al.*[23] and Lu *et al.*[24] in their studies of internal swirling flows. A small flow oscillation arising in a shear layer tends to seek a specific acoustic mode to interact, so long as the *lock-in* requirements are fulfilled. In addition to the vortex shedding in the wake of the first guide vane, there may exist other mechanisms for exciting acoustic motions in the injector. For example, the helical mode of hydrodynamic instability may drive the first-tangential mode of the acoustic field. The outer shear layer may trigger the first-radial mode of the acoustic wave for certain injection geometries and flow conditions.

2. High swirl number

Figure 22 shows the azimuthal velocity fields of the first six POD modes on a longitudinal (x–r) plane for the high swirl-number case. The corresponding frequency contents given in Fig. 23 reveal a much broader distribution compared with the low swirl-number case. The first mode only accounts for 6.8% of the total energy, as indicated in Fig. 24. As a result of the strong swirling effect, the large-scale motion in the central recirculation zone dominates the flow development, with a characteristic frequency of 4000 Hz. The interactions between the shear layer downstream of the first guide vane and the central recirculating flow also play a

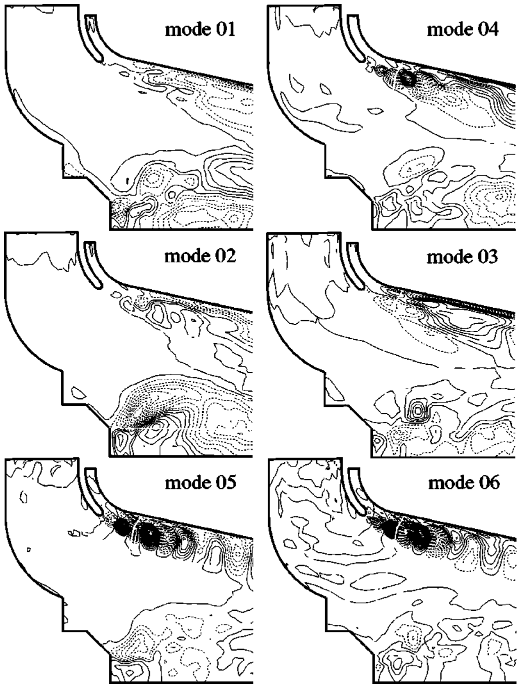

FIG. 22. Spatial distributions of first six POD modes (azimuthal velocity fields) on longitudinal (x–r) plane, high swirl number (S=0.49). Contour levels between −1000 and 1000 m/s with increment of 50 m/s. Solid lines: positive values; dashed lines: negative values.

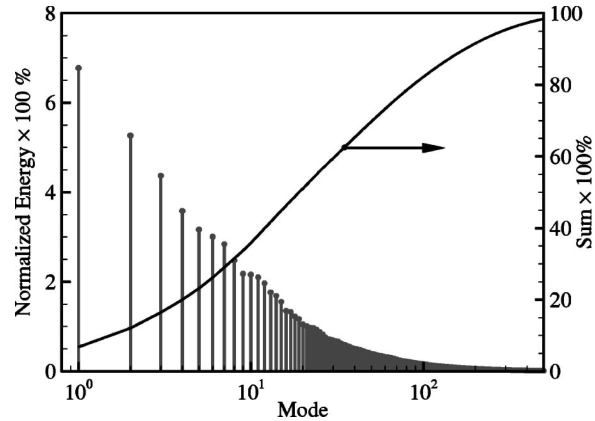

FIG. 24. Energy distribution of POD modes on longitudinal (x–r) plane, high swirl number (S=0.49).

prevalent role in the first four modes, with a characteristic frequency around 1500 Hz. The fifth and sixth modes are closely related to the streamwise Kelvin–Helmholtz instabilities downstream of the first guide vane, with a dominant frequency around 1.4×10^4 Hz. Their spatial distributions are almost identical to the first two modes in the low swirl-number case, but the energy level is severely suppressed under the effects of the vortex-breakdown-induced recirculating flow in the center region.

Figure 25 shows the mode shapes on the transverse plane at x=15 mm. The alternating organized structures in the outer shear layer results from the Kelvin–Helmholtz instability in the azimuthal direction downstream of the first guide vane. A dipole structure clearly exists near the centerline in the first two modes, which transits to a quadrupole structure in the fourth and fifth modes. This kind of helical motion represents intrinsic flow instabilities associated with the precession of the vortex core. They are decoupled from the injector acoustic field since the characteristic frequencies (2000 Hz for the first two POD modes and 4000 Hz for the fourth and fifth modes)[18] are much smaller than that of the lowest transverse acoustic mode in the injector (i.e., around 5000 Hz for the first tangential mode).

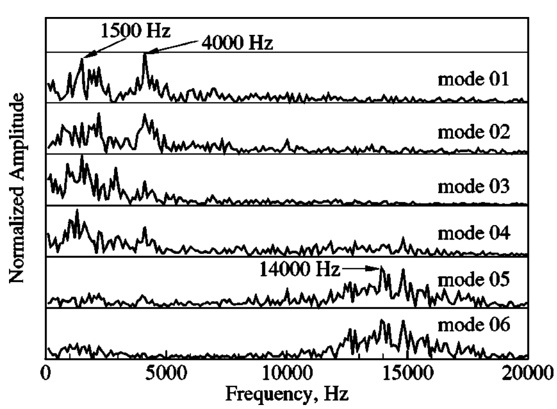

FIG. 23. Frequency spectra of temporal variations of first six POD modes, high swirl number (S=0.49).

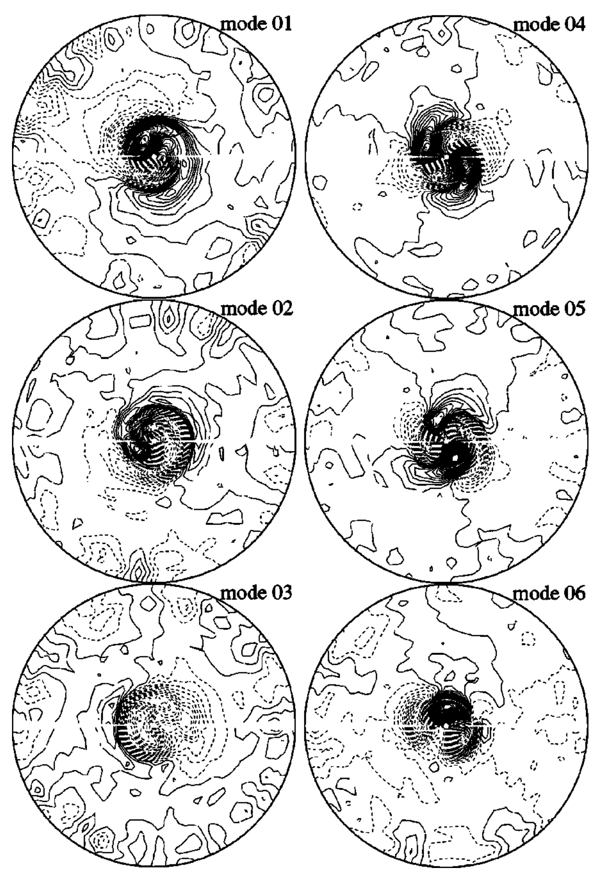

FIG. 25. Spatial distributions of first six POD modes (pressure contours) on transverse plane, high swirl number (S=0.49). Contour levels between −60 000 and 60 000 Pa with increment of 2500 Pa. Solid lines: positive values; dashed lines: negative values.

VI. CONCLUSIONS

A comprehensive numerical analysis has been conducted to investigate the vortical flow dynamics in a swirl injector with radial entry. The formulation treats the Favre-filtered conservation equations in three dimensions, with turbulence closure achieved using a large-eddy-simulation technique. Various fundamental mechanisms dictating the flow evolution, including vortex breakdown, Kelvin–Helmholtz instability, and helical instability, as well as their interactions, were examined systematically for different swirl numbers. Two distinct flow regions exist in the injector: the outer shear layer, induced by the Kelvin–Helmholtz instability, and the central toroidal recirculation zone, caused by vortex breakdown. The swirl number plays an important role in determining the injector dynamics. In the low swirl-number case, the vortex shedding in the outer shear layer attunes the flow oscillation in the bulk of the injector with a frequency of 1.3×10^4 Hz, whereas the central recirculating flow precesses around the centerline at 5.7×10^3 Hz. A bulb type of double vortex breakdown is clearly observed in the downstream region of the centerbody. The flow structures become much more complicated with increasing swirl number. Higher swirl velocity enhances the central recirculating flow as well as the unsteady motion in the azimuthal direction, and subsequently suppresses the development of the streamwise instability in the outer shear-layer region. The interactions among flow evolution process in various parts of the injector also become stronger. As a result, the vortex breakdown phenomena cannot be defined using a simple classification scheme.

ACKNOWLEDGMENTS

This work was sponsored by the NASA Glenn Research Center under Grant No. NAG 3-2151. The support and encouragement from Kevin Breisacher is greatly appreciated. The authors are grateful for technical discussions with Dr. Jeff Cohen of United Technologies Research Center.

[1] *Liquid Rocket Engine Combustion Instability*, edited by V. Yang and W. Anderson, Progress in Aeronautics and Astronautics, Vol. 169 (AIAA, Reston, VA, 1995).
[2] T. Lieuwen and K. McManus, "Introduction: Combustion dynamics in lean-premixed prevaporized (LPP) gas turbines," J. Propul. Power **19**, 721 (2003).
[3] F. E. C. Culick and V. Yang, "Overview of combustion instabilities in liquid propellant rocket engines," in Ref. 1, pp. 3–37.
[4] S. V. Apte, K. Mahesh, P. Moin, and J. C. Oefelein, "Large-eddy simulation of swirling particle-laden flows in coaxial-jet combustors," Int. J. Multiphase Flow **29**, 1311 (2003).
[5] C. D. Pierce and P. Moin, "Progress-variable approach for large-eddy simulation of non-premixed turbulent combustion," J. Fluid Mech. **504**, 73 (2004).
[6] Y. Huang and V. Yang, "Effect of swirl on combustion dynamics in lean-premixed swirl-stabilized combustor," Proc. Combust. Inst. **30**, 1775 (2005).
[7] V. G. Bazarov and V. Yang, "Liquid-propellant rocket engine injector dynamics," J. Propul. Power **14**, 797 (2002).
[8] C. B. Graves, "Outer shear layer swirl mixer for a combustor," US Patent 5-603-211, 1997.
[9] S. Wang and V. Yang, "Unsteady flow evolution in swirl injectors with radial entry. II. External excitations," Phys. Fluids **17**, 045107 (2005).
[10] G. Erlebacher, M. Y. Hussaini, C. G. Speziale, and T. A. Zang, "Toward the large eddy simulation of compressible turbulent flows," J. Fluid Mech. **238**, 155 (1992).
[11] J. Smagorinsky, "General circulation experiments with the primitive equations. I. The basic experiment," Mon. Weather Rev. **91**, 99 (1963).
[12] A. Yoshizawa, "Statistical theory for compressible turbulent shear flows, with the applications to subgrid modeling," Phys. Fluids **29**, 2152 (1986).
[13] U. Piomelli, P. Moin, and J. H. Ferziger, "Model consistency in large eddy simulation of turbulent channel flows," Phys. Fluids **31**, 1884 (1988).
[14] T. A. Zang, R. B. Dahlburg, and J. P. Dahlburg, "Direct and large-eddy simulations of three-dimensional compressible Navier–Stokes turbulence," Phys. Fluids A **4**, 127 (1992).
[15] M. P. Martín, U. Piomelli, and G. V. Candler, "Subgrid-scale models for compressible large-eddy simulations," Theor. Comput. Fluid Dyn. **13**, 361 (2000).
[16] U. Piomelli, "Large-eddy simulation: Achievements and challenges," Prog. Aerosp. Sci. **35**, 335 (1999).
[17] T. J. Poinsot and S. K. Lele, "Boundary conditions for direct simulations of compressible viscous flows," J. Comput. Phys. **101**, 104 (1992).
[18] S. Wang, "Vortical flow dynamics and acoustic response of gas-turbine swirl-stabilized injectors," Ph.D. thesis, Pennsylvania State University, University Park, PA, 2002.
[19] Y. Fabignon, R. A. Beddini, and Y. Lee, "Analytic evaluation of finite difference methods for compressible direct and large eddy simulations," Aerospace Sci. Technol. **6**, 413 (1997).
[20] S. Apte and V. Yang, "Unsteady flow evolution in porous chamber with surface mass injection, part 1: Free oscillation," AIAA J. **39**, 1577 (2001).
[21] M. M. Rai and S. Chakravarthy, "Conservative high-order accurate finite difference method for curvilinear grids," AIAA Pap. 93-3380 (1993).
[22] S. Apte and V. Yang, "An LES study of transition and flow instability in a porous-walled chamber with mass injection," J. Fluid Mech. **447**, 215 (2003).
[23] Y. Huang, H. G. Sung, S. H. Hsieh, and V. Yang, "Large eddy simulation of combustion dynamics of a lean-premixed swirl-stabilized combustor," J. Propul. Power **19**, 722 (2003).
[24] X. Lu, S. Wang, H. G. Sung, S. H. Hsieh, and V. Yang. "Large eddy simulation of turbulent swirling flows injected into a dump chamber," J. Fluid Mech. **527**, 171 (2005).
[25] S. C. Favaloro, A. S. Nejad, S. A. Ahmed, S. P. Vanka, and T. J. Miller, "An experimental and computational investigation of isothermal swirling flow in an axisymmetric dump combustor," AIAA Pap. 89-0620 (1989).
[26] G. I. Taylor, "The spectrum of turbulence," Proc. R. Soc. London, Ser. A **164**, 476 (1938).
[27] S. B. Pope, *Turbulent Flows* (Cambridge University Press, Cambridge, 2000).
[28] V. Shtern and F. Hussain, "Collapse, symmetry, breaking, and hysteresis in swirling flows," Annu. Rev. Fluid Mech. **31**, 537 (1999).
[29] C.-M. Ho and P. Huerre, "Perturbed free shear layers," Annu. Rev. Fluid Mech. **16**, 365 (1984).
[30] M. Lessen, P. J. Singh, and F. Paillet, "The stability of a trailing line vortex. 1. Inviscid theory," J. Fluid Mech. **360**, 753 (1974).
[31] J. E. Martin and E. Meiburg, "Nonlinear axisymmetric and three-dimensional vorticity dynamics in a swirling jet model," Phys. Fluids **8**, 1917 (1996).
[32] A. K. Gupta, D. G. Lilley, and N. Syred, *Swirl Flows* (Abacus, Kent, 1984).
[33] O. Lucca-Negro and T. O'Doherty, "Vortex breakdown: A review," Prog. Energy Combust. Sci. **27**, 431 (2001).
[34] C. W. Rowley, T. Colonius, and R. M. Murray, "Model reduction for compressible flows using pod and Galerkin projection," Physica D **189**, 115 (2004).
[35] G. Berkooz, P. Holmes, and J. L. Lumley, "The proper orthogonal decomposition in the analysis of turbulent flows," Annu. Rev. Fluid Mech. **25**, 539 (1993).